

1 **Bimodal or quadrimodal? Statistical tests for the shape of fault patterns**

2 David Healy^{1*} & Peter Jupp²

3 ¹School of Geosciences, King's College, University of Aberdeen, Aberdeen AB24 3UE Scotland

4 ²School of Mathematics & Statistics, University of St Andrews, St Andrews KY16 9SS Scotland

5 *Corresponding author e-mail: d.healy@abdn.ac.uk

6

7 **Abstract**

8 Natural fault patterns, formed in response to a single tectonic event, often display significant
9 variation in their orientation distribution. The cause of this variation is the subject of some
10 debate: it could be 'noise' on underlying conjugate (or bimodal) fault patterns or it could be
11 intrinsic 'signal' from an underlying polymodal (e.g. quadrimodal) pattern. In this contribution,
12 we present new statistical tests to assess the probability of a fault pattern having two (bimodal,
13 or conjugate) or four (quadrimodal) underlying modes and orthorhombic symmetry. We use
14 the eigenvalues of the 2nd and 4th rank orientation tensors, derived from the direction cosines
15 of the poles to the fault planes, as the basis for our tests. Using a combination of the existing
16 fabric eigenvalue (or modified Flinn) plot and our new tests, we can discriminate reliably
17 between bimodal (conjugate) and quadrimodal fault patterns. We validate our tests using
18 synthetic fault orientation datasets constructed from multimodal Watson distributions, and
19 then assess six natural fault datasets from outcrops and earthquake focal plane solutions. We
20 show that five out of six of these natural datasets are probably quadrimodal and orthorhombic.
21 The tests have been implemented in the R language and a link is given to the authors' source
22 code.

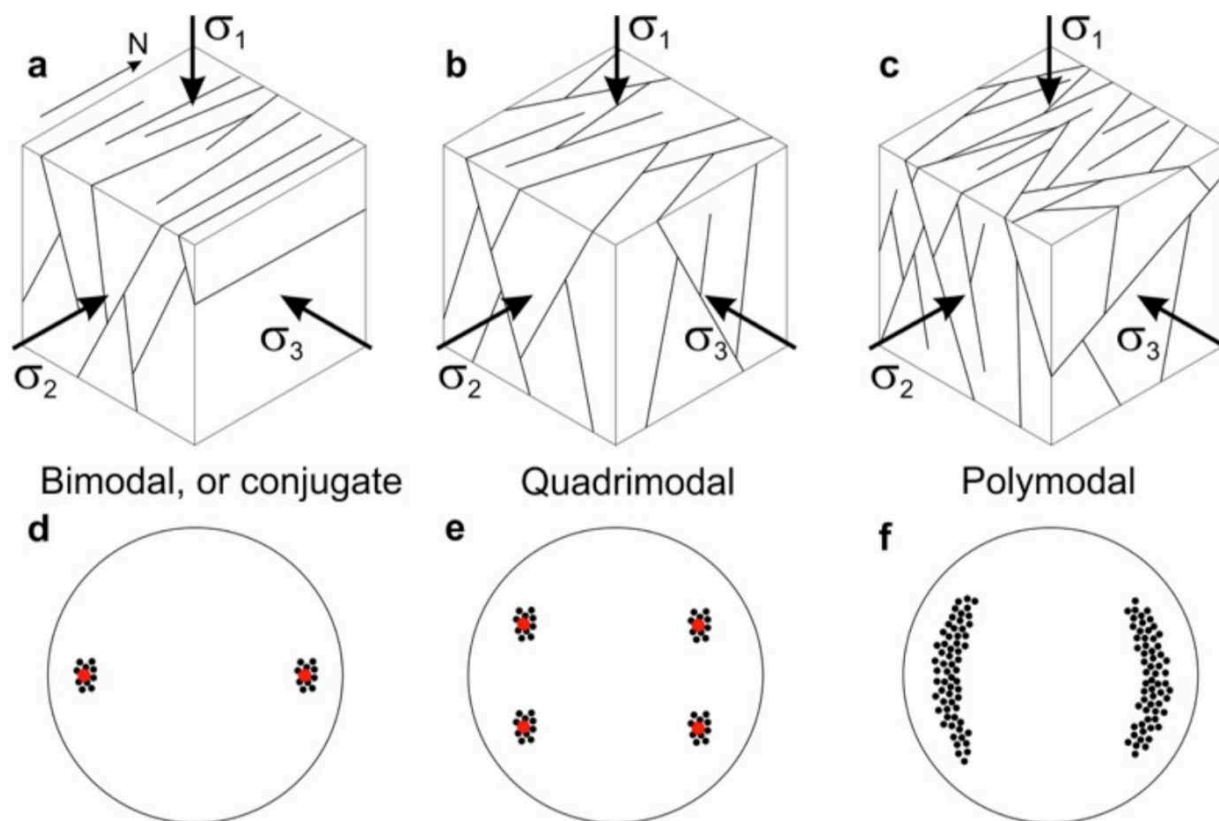
23

24 **1. Introduction**

25 *1.1 Background*

26 Faults are common structures in the Earth's crust, and they rarely occur in isolation. Patterns
27 of faults, and other fractures such as joints and veins, control the bulk transport and mechanical
28 properties of the crust. For example, arrays of low permeability (or 'sealing') faults in a rock
29 matrix of higher permeability can produce anisotropy of permeability and preferred directions
30 of fluid flow. Arrays of weak faults can similarly produce anisotropy – i.e. directional variations
31 – of bulk strength. It is important to understand fault patterns, and quantifying the geometrical
32 attributes of any pattern is an important first step. Faults, taken as a class of brittle shear
33 fractures, are often assumed to form in conjugate arrays, with fault planes more or less evenly
34 distributed about the largest principal compressive stress, σ_1 , and making an acute angle with
35 it. This model, an amalgam of theory and empirical observation, predicts that conjugate fault
36 planes intersect along the line of σ_2 (the intermediate principal stress) and the fault pattern
37 overall displays bimodal symmetry (Figure 1a). A fundamental limitation of this model is that
38 these fault patterns can only ever produce a plane strain (intermediate principal strain $\epsilon_2 = 0$),

39 with no extension or shortening in the direction of σ_2 . This kinematic limitation is inconsistent
 40 with field and laboratory observations that document the existence of polymodal or
 41 quadrimodal fault patterns, and which produce triaxial strains in response to triaxial stresses
 42 (e.g. Aydin & Reches, 1982; Reches, 1978; Blenkinsop, 2008; Healy et al., 2015; McCormack &
 43 McClay, 2018). Polymodal and quadrimodal fault patterns possess orthorhombic symmetry
 44 (Figure 1b & 1c).



45

46 **Figure 1.** Schematic diagrams to compare conjugate fault patterns displaying bimodal
 47 symmetry with quadrimodal and polymodal fault patterns displaying orthorhombic symmetry.
 48 **a-c)** Block diagrams showing patterns of normal faults and their relationship to the principal
 49 stresses. **d-f)** Stereographic projections (equal area, lower hemisphere) showing poles to fault
 50 planes for the models shown in a-c. Natural examples of all three patterns have been found in
 51 naturally deformed rocks.

52 Fault patterns are most often visualised through maps of their traces and equal-angle
 53 (stereographic) or equal-area projections of poles to fault planes or great circles. Azimuthal
 54 projection methods (hereafter 'stereograms') provide a measure of the orientation distribution,
 55 including the attitude and the shape of the overall pattern. However, these plots can be
 56 unsatisfactory when they contain many data points, or the data are quite widely dispersed.
 57 Woodcock (1977) developed the idea of the fabric shape, based on the fabric or orientation
 58 tensor of Scheidegger (1965). The eigenvalues of this 2nd rank tensor can be used in a modified
 59 Flinn plot (Flinn, 1962; Ramsay, 1967) to discriminate between clusters and girdles of poles.
 60 These plots can be useful for three of the five possible fabric symmetry classes – spherical, axial
 61 and orthorhombic – because the three fabric eigenvectors coincide with the three symmetry
 62 axes. However, there are issues with the interpretation of distributions that are not uniaxial

63 (Woodcock, 1977). We address these issues in this paper. Reches (Reches, 1978; Aydin &
64 Reches, 1982; Reches, 1983; Reches & Dieterich, 1983) has exploited the orthorhombic
65 symmetry of measured quadrimodal fault patterns to explore the relationship between their
66 geometric/ kinematic attributes and tectonic stress. More recently, Yielding (2016) measured
67 the branch lines of intersecting normal faults from seismic reflection data and found they
68 aligned with the bulk extension direction – a feature consistent with their formation as
69 polymodal patterns. Bimodal (i.e. conjugate) fault arrays have branch lines aligned
70 perpendicular to the bulk extension direction.

71 *1.2 Rationale*

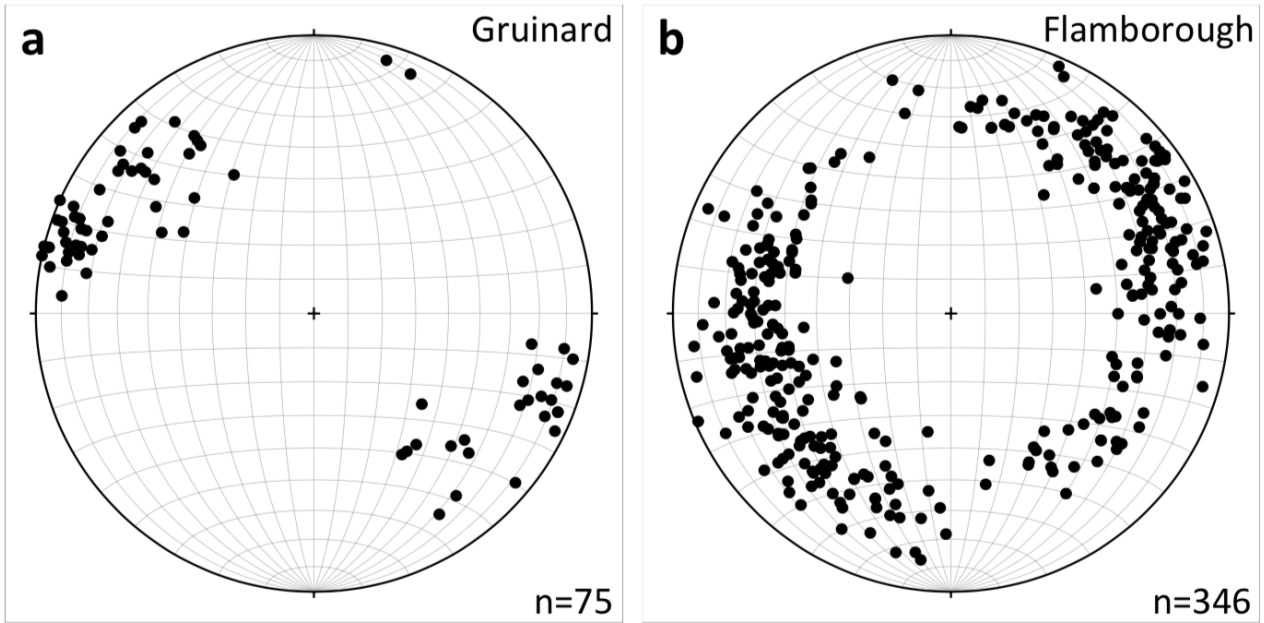
72 The fundamental underlying differences in the symmetries of the two kinds of fault pattern –
73 (i) bimodal and bilateral or (ii) and polymodal and orthorhombic – suggest that we should test
74 for this symmetry using the orientation distributions of measured fault planes. The results of
75 such tests may provide further insight into the kinematics and/or dynamics of the fault-forming
76 process. This paper describes new tests for fault pattern orientation data, and includes the
77 program code for each test written in the R language (R Core Team, 2017). The paper is
78 organised as follows: the next section (2) reviews the kinematic and mechanical issues raised
79 by conjugate and polymodal fault patterns, and in particular, the implications for their
80 orientation distributions. Section 3 describes the datasets used in this study, including
81 synthetic and natural fault orientation distributions. Section 4 presents tests for assessing
82 whether an orientation distribution has orthorhombic symmetry, including a description of the
83 mathematics and the R code. The examples used include synthetic orientation datasets of
84 known attributes (with and without added ‘noise’) and natural datasets of fault patterns
85 measured in a range of rock types. A Discussion of issues raised is provided in Section 5, and is
86 followed by a short Summary. The R code is available from [http://www.mcs.st-](http://www.mcs.st-andrews.ac.uk/~pej/2mode_tests.html)
87 [andrews.ac.uk/~pej/2mode_tests.html](http://www.mcs.st-andrews.ac.uk/~pej/2mode_tests.html)

88

89 **2. Bimodal (conjugate) versus quadrimodal fault patterns**

90 Conjugate fault patterns should display bimodal or bilateral symmetry in their orientation
91 distributions on a stereogram, and ideally show evidence of central tendency about these two
92 clusters (Figure 1d; Healy et al., 2015). Quadrimodal fault patterns should show orthorhombic
93 symmetry and, ideally, evidence of central tendency about the four clusters of poles on
94 stereograms (Figure 1e). More general polymodal patterns should show orthorhombic
95 symmetry with an even distribution of poles in two arcs (Figure 1f). For data collected from
96 natural fault planes some degree of intrinsic variation, or ‘noise’, is to be expected. Two natural
97 example datasets are shown in Figure 2. The Gruinard dataset is from a small area (~ 5 m²) in
98 one outcrop of Triassic sandstone, and shows poles to deformation bands with small normal
99 offsets (mm-cm). The Flamborough dataset is taken from Peacock & Sanderson (1992; their
100 Figure 2a) and shows poles to normal faults in the Cretaceous chalk along a coastline section of
101 about 1.8 km. The authors clearly state that the approximately E-W orientation of the coastline
102 may have generated a sampling bias in the measured data (i.e. a relative under-representation
103 of E-W oriented fault planes). Both datasets illustrate the nature of the problem addressed in

104 this paper: given variable, incomplete and noisy data of different sample sizes, how can we
105 assess the symmetry of the underlying fault pattern?



106

107 **Figure 2.** Stereographic projections (equal area, lower hemisphere) showing two natural fault
108 datasets. a) Poles to deformation bands (small offset faults; $n=75$) measured in Triassic
109 sandstones at Gruinard Bay, NW Scotland (Healy et al., 2006a, b). These data were collected
110 from a small contiguous outcrop, approximately 10 m² in area. b) Poles to faults measured in
111 Cretaceous chalk at Flamborough Head, NE England ($n=346$). These data have been taken from a
112 figure published in Peacock & Sanderson (1992) and re-plotted in the same format as those
113 from Gruinard.

114

115 3. Datasets used in this study

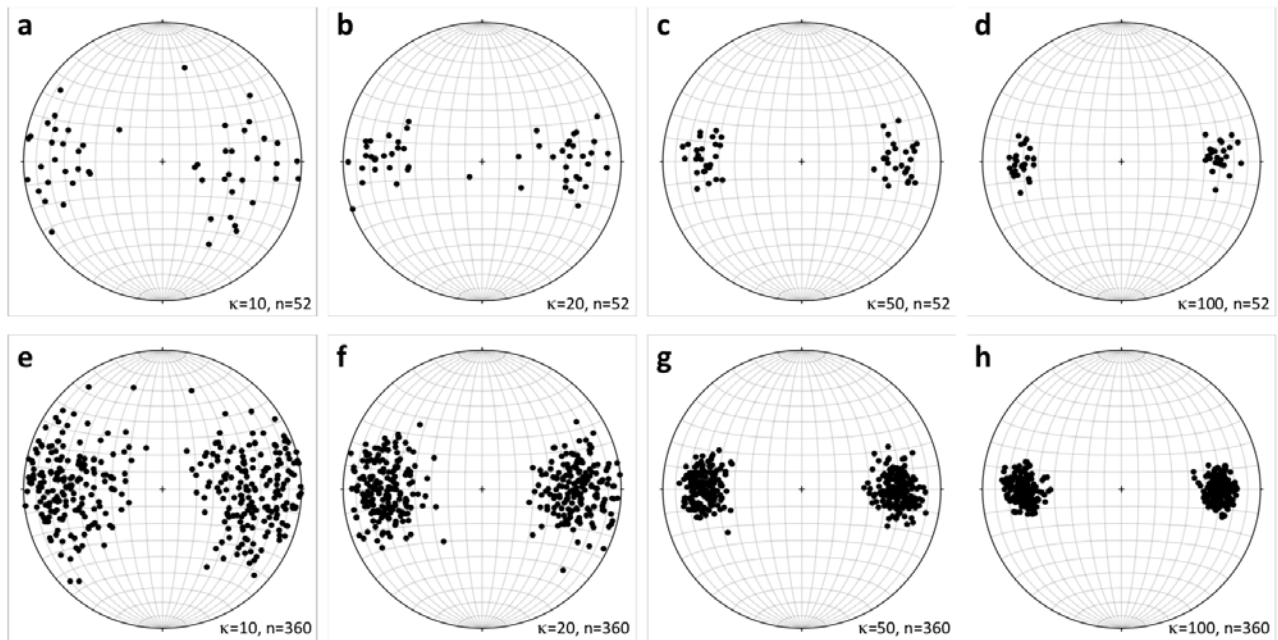
116 3.1. Synthetic datasets

117 We use two sets of synthetic data to test our new statistical methods, both based on the Watson
118 orientation distribution (Fisher et al., 1987 section 4.4.4; Mardia & Jupp, 2000 section 9.4.2).
119 This is the simplest non-uniform distribution for describing undirected lines, and has
120 probability density

$$121 f(\pm\mathbf{x}; \boldsymbol{\mu}, \kappa) \propto \exp\{\kappa(\boldsymbol{\mu}^T \mathbf{x})^2\}$$

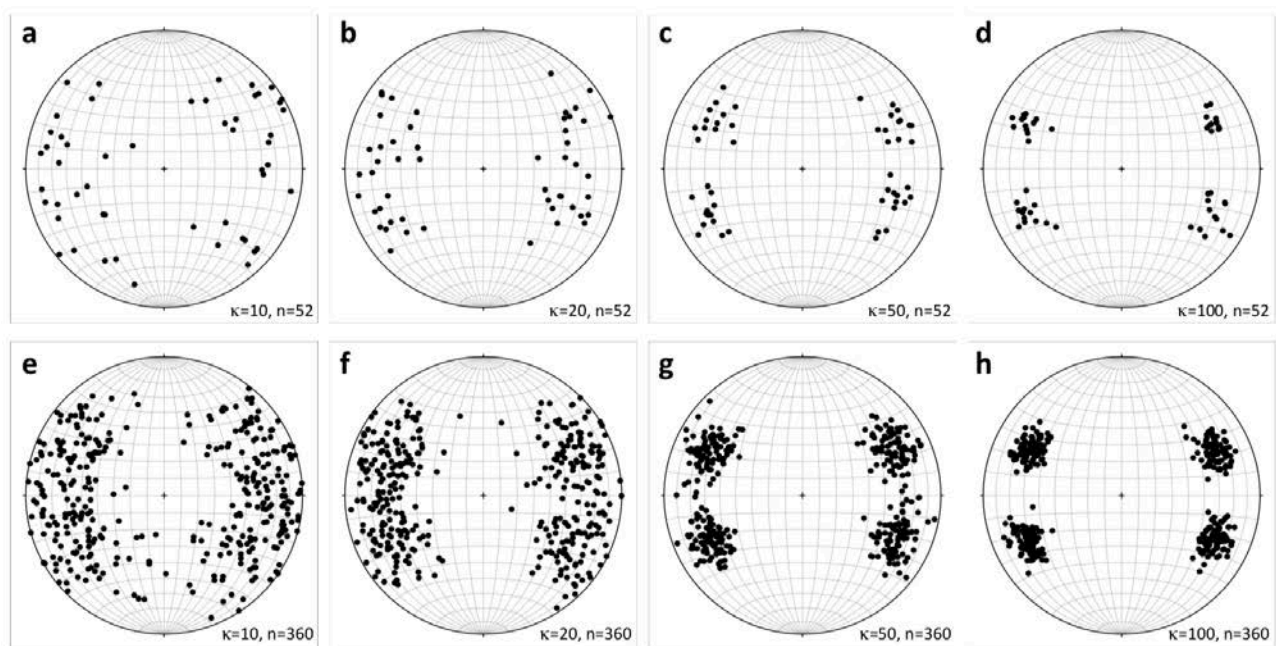
122 where κ is a measure of concentration (low κ = dispersed, high κ = concentrated) and $\boldsymbol{\mu}$ is the
123 mean direction. To obtain a synthetic conjugate fault pattern dataset of size n we combined two
124 datasets of size $n/2$, each from a Watson distribution, the two mean directions being separated
125 by 60°. We generated synthetic bimodal datasets with $\kappa = 10, 20, 50$ and 100 and $n=52$ and 360
126 (Figure 3). This variation in κ provides a useful range of concentrations encompassing those
127 observed in measured natural data, and can be considered as a measure of 'noise' within the
128 distribution. Many natural datasets are often small due to limitations of outcrop size, and the

129 two sizes of synthetic distribution ($n=52$ and 360) allow for this fact. For synthetic polymodal
130 fault patterns, we generated quadrimodal datasets of size n by combining four Watson
131 distributions of size $n/4$ with their mean directions separated by 60° in dip (as above) and 52°
132 in strike (see Healy et al., 2006a, b). By varying n from 52 to 360 we cater for comparisons with
133 smaller and larger natural datasets, and as for the synthetic bimodal datasets, we varied κ in
134 the range 10, 20, 50 and 100 (Figure 4).



135
136 **Figure 3.** Stereographic projections (equal area, lower hemisphere) showing the eight
137 synthetic datasets designed to model conjugate (bimodal) fault patterns in this study. **a-d)**
138 Synthetic fault datasets derived from equal mixtures of two Watson distributions with mean
139 pole directions separated by an inter-fault dip angle of 60 degrees. These models represent a
140 'low fault count' scenario, with $n = 52$ and κ (the Watson dispersion parameter) varying from
141 10 to 100. **e-h)** These models represent a 'high fault count' scenario, with $n = 360$ and κ varying
142 from 10 to 100.

143



144

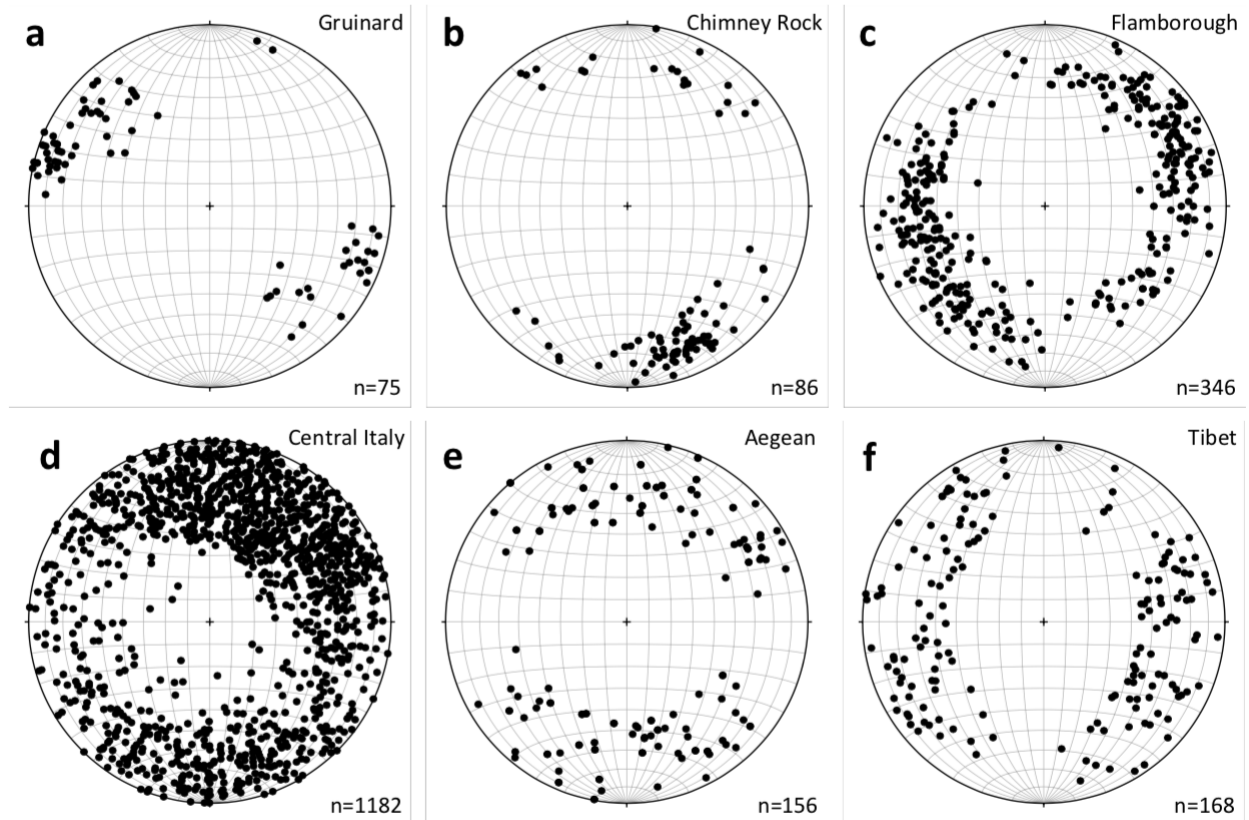
145 **Figure 4.** Stereographic projections (equal area, lower hemisphere) showing the eight
 146 synthetic datasets designed to model quadrimodal fault patterns in this study. **a-d)** Synthetic
 147 fault datasets derived from equal mixtures of four Watson distributions with mean pole
 148 directions separated by an inter-fault dip angle of 60 degrees and a strike separation of 52
 149 degrees. These models represent a 'low fault count' scenario, with $n = 52$ and κ (the Watson
 150 dispersion parameter) varying from 10 to 100. **e-h)** These models represent a 'high fault count'
 151 scenario, with $n = 360$ and κ varying from 10 to 100.

152

153 3.2. Natural datasets

154 We use six natural datasets of fault plane orientations from regions that have undergone or are
 155 currently undergoing extension - i.e. we believe the majority of these faults display normal
 156 kinematics (Figure 5). The Gruinard dataset (Figure 5a) is from Gruinard Bay in NW Scotland
 157 (UK), and featured in previous publications (Healy et al., 2006a, b). The most important thing
 158 about this dataset is that the fault planes were all measured from a small area ($\sim 5 \text{ m}^2$) of
 159 contiguous outcrop of a single sandstone bed. This means it is highly unlikely that the
 160 orientation data are affected by any local stress variations and subsequent possible rotations.
 161 The data were measured in normal-offset deformation bands with displacements of a few
 162 millimetres to centimetres. The next three datasets have been digitised from published papers
 163 on normal faults in Utah (Figure 5b; Chimney Rock; Krantz, 1989), northern England (Figure
 164 5c; Flamborough; Peacock & Sanderson, 1992) and Italy (Figure 5d; Central Italy; Roberts,
 165 2007). In each case, the published stereograms were digitised to extract Cartesian (x,y)
 166 coordinates of the poles to faults, and these were then converted to plunge and plunge direction
 167 using the standard equations for the projection used (e.g. Lisle & Leyshon, 2004). Slight
 168 differences in the number of data plotted for each of these three with respect to the original
 169 publication arise due to the finite resolution of the digitised image of the stereograms. The last
 170 two datasets for the Aegean and Tibet (Figure 5e & f) are derived from earthquake focal
 171 mechanisms using the CMT catalogue (Ekström et al., 2012). In each case the steepest dipping

172 nodal plane was selected in the absence of convincing evidence for low-angle normal faulting
173 in these regions.



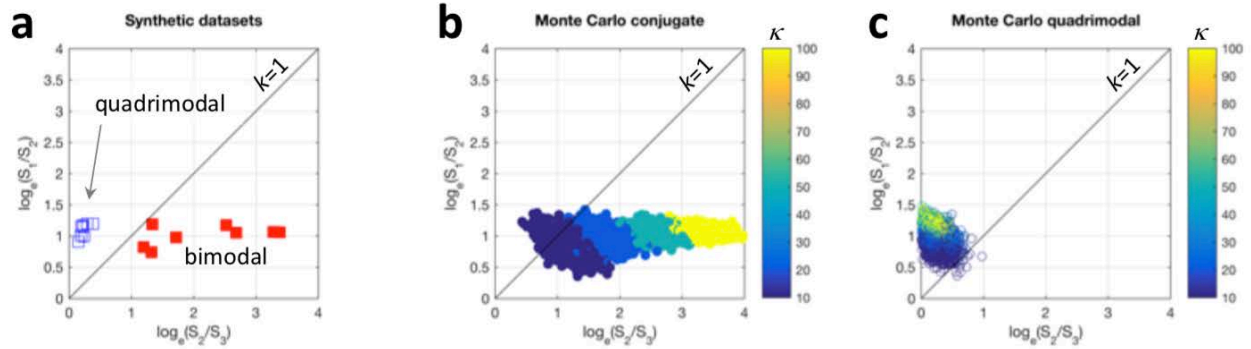
174

175 **Figure 5.** Stereographic projections (equal area, lower hemisphere) showing the six natural
176 datasets used in this study. All plots show poles to faults, the majority of which are inferred to
177 be normal. **a)** Data from deformation bands measured in faulted Triassic sandstones at
178 Gruinard Bay, Scotland (Healy et al., 2006a; 2006b). **b)** Data from faults and measured in
179 sandstones at Chimney Rock in the San Rafael Swell, Utah, USA. Data digitised from Krantz
180 (1989). **c)** Data from faults measured in cliffs of Cretaceous chalk at Flamborough Head, NE
181 England. Data digitised from Peacock & Sanderson (1992). **d)** Data from faults measured in the
182 Apennines of Central Italy. Data digitised from Roberts (2007). **e)** Data from focal mechanism
183 nodal planes derived from the CMT catalogue for the Aegean region (Ekström et al., 2012). **f)**
184 Data from focal mechanism nodal planes derived from the CMT catalogue for the Tibet region
185 (Ekström et al., 2012).

186

187 4. Testing for orthorhombicity

188 4.1 Eigenvalue fabric (modified Flinn) plots



189

190 **Figure 6.** Graphs showing the ratios of eigenvalues of the orientation matrices for the synthetic
 191 datasets (Flinn, 1962; Ramsay, 1967; Woodcock, 1977). **a)** Synthetic conjugate (i.e. bimodal;
 192 filled red symbols) and quadrimodal (hollow blue symbols) fault data. Note that the conjugate
 193 and quadrimodal data lie either side of the line $k = 1$, where $k = \log_e(S_1/S_2)/\log_e(S_2/S_3)$. **b)**
 194 Eigenvalue ratios from a Monte Carlo simulation of conjugate fault orientations using the two
 195 Watson mixture model. 1000 simulations were run for each of four different κ values (10, 20,
 196 50 and 100; a total of 4000 data points), corresponding to the range of the discrete datasets
 197 shown in a). **c)** Eigenvalue ratios from a Monte Carlo simulation of quadrimodal fault
 198 orientations using the four Watson mixture model. 1000 simulations were run for each of four
 199 different κ values (10, 20, 50 and 100; a total of 4000 data points), corresponding to the range
 200 of the discrete datasets shown in a).

201 We calculated the 2nd rank orientation tensor (Woodcock, 1977) for each of the synthetic
 202 datasets shown in Figures 3 and 4 (bimodal and quadrimodal, respectively). The eigenvalues of
 203 this tensor (S_1 , S_2 and S_3 , where S_1 is the largest and S_3 is the smallest) are used to plot the data
 204 on a modified Flinn diagram (Figure 6), with $\log_e(S_2/S_3)$ on the x -axis and $\log_e(S_1/S_2)$ on the y -
 205 axis. The points corresponding to the bimodal (shown in red) and quadrimodal (shown in blue)
 206 datasets lie in distinct areas. Bimodal (conjugate) fault patterns lie below the 1:1 line, on which
 207 $S_1/S_2 = S_2/S_3$. This is due to the S_3 eigenvalue being very low (near 0) for these distributions,
 208 which for high values of κ begin to resemble girdle fabric patterns confined to the plane of the
 209 eigenvectors corresponding to eigenvalues S_1 and S_2 (Woodcock, 1977). In contrast, the
 210 quadrimodal patterns lie above the 1:1 line, as S_3 for these distributions is large relative to the
 211 equivalent bimodal pattern (i.e. for the same values of κ and n). The modified Flinn plot
 212 therefore provides a potentially rapid and simple way to discriminate between bimodal
 213 (conjugate) and quadrimodal fault patterns. Note, however, that the spread of the bimodal
 214 patterns in Figure 6a along the x -axis is a function of the κ value of the underlying Watson
 215 distribution, with low values of κ – low concentration, highly dispersed – lying closer to the
 216 origin. Dispersed or noisy bimodal (conjugate) patterns may therefore lie closer to
 217 quadrimodal patterns (see Discussion below).

218 4.2 Randomisation tests using 2nd and 4th rank orientation tensors

219 4.2.1 Underlying distributions

220 To get a suitable general setting for our tests, we formalise the construction of the bimodal and
 221 quadrimodal datasets considered in Section 3.1. Whereas the datasets considered in Section 3.1

222 necessarily have equal numbers of points around each mode, for datasets arising from the
 223 distributions here, this is true *only on average*. The very restrictive condition of having a
 224 Watson distribution around each mode is relaxed here to that of having a circularly-symmetric
 225 distribution around each mode.

226 Suppose that axes $\pm\mathbf{x}_1, \dots, \pm\mathbf{x}_n$ are independent observations from some distribution of axes. If
 227 the parent distribution is thought to be multi-modal then two appealing models are:

228 (i) The **bimodal equal mixture model** can be thought of intuitively as obtained by ‘pulling
 229 apart’ a unimodal distribution into two equally strong modes angle α apart. More precisely,
 230 the probability density is:

$$231 \quad f_2(\pm\mathbf{x}; \{\pm\boldsymbol{\mu}_1, \pm\boldsymbol{\mu}_2\}) = \frac{1}{2}\{g(\pm\mathbf{x}; \pm\boldsymbol{\mu}_1) + g(\pm\mathbf{x}; \pm\boldsymbol{\mu}_2)\}, \quad (1)$$

232 where $\pm\boldsymbol{\mu}_1$ and $\pm\boldsymbol{\mu}_2$ are axes angle α apart, and $g(\cdot; \pm\boldsymbol{\mu})$ is the probability density function of
 233 some axial distribution that has rotational symmetry about its mode $\pm\boldsymbol{\mu}$;

234 (ii) The **quadrимodal equal mixture model** can be thought of intuitively as obtained by
 235 ‘pulling apart’ a bimodal equal mixture distribution into two bimodal equal
 236 mixture distributions with planes angle γ apart, so that it has four equally strong modes.
 237 More precisely, the probability density is:

$$238 \quad f_4(\pm\mathbf{x}; \{\pm\boldsymbol{\mu}_1, \pm\boldsymbol{\mu}_2\}, \gamma) = \frac{1}{4}\sum_{\epsilon, \eta} g(\pm\mathbf{x}; \pm\boldsymbol{\mu}_{\epsilon, \eta}), \quad (2)$$

239 where

$$240 \quad \boldsymbol{\mu}_{\epsilon, \eta} = \check{c}(c\mathbf{v}_1 + \epsilon s\mathbf{v}_2) + \eta \check{s}\mathbf{v}_3 \quad (3)$$

241 with $c = \cos(\alpha/2)$, $s = \sin(\alpha/2)$, $\check{c} = \cos(\gamma/2)$, $\check{s} = \sin(\gamma/2)$, $\cos(\alpha) = \boldsymbol{\mu}'_1\boldsymbol{\mu}_2$ and (ϵ, η) runs
 242 through $\{\pm 1\}^2$. If $\gamma = 0$, then (3) reduces to (2).

243 The problem of interest is to decide whether the parent distribution is (1) or (2).

244

245 4.2.2 The tests

246 Given axes $\pm\mathbf{x}_1, \dots, \pm\mathbf{x}_n$ we denote by $\pm\hat{\mathbf{v}}_1$ and $\pm\hat{\mathbf{v}}_3$, respectively, the principal axes of the
 247 orientation tensor corresponding to the largest and smallest eigenvalues, S_1 and S_3 . We can also
 248 define

$$249 \quad S_{11} = n^{-1}\sum_{i=1}^n(\hat{\mathbf{v}}'_1\mathbf{x}_i)^4, S_{33} = n^{-1}\sum_{i=1}^n(\hat{\mathbf{v}}'_3\mathbf{x}_i)^4.$$

250 S_1 and S_3 are the 2nd moments of $\pm\mathbf{x}_1, \dots, \pm\mathbf{x}_n$ along the 1st and 3rd principal axes, respectively,
 251 whereas S_{11} and S_{33} are the 4th moments along these principal axes. Therefore, both $S_1 - S_3$ and
 252 $S_{11} - S_{33}$ are measures of anisotropy of $\pm\mathbf{x}_1, \dots, \pm\mathbf{x}_n$.

253 Some algebra shows that

$$254 \quad T_1 - T_3 = \cos(\gamma)\{E[x^2] - E[v^2]\}, \quad (4)$$

255 where T_1 and T_3 are the population versions of S_1 and S_3 , respectively, and $\pm x$ and $\pm v$ are the
 256 components of $\pm \mathbf{x}$ in the quadrimodal equal mixture model (2) along its 1st and 3rd principal
 257 axes, respectively. Then (4) gives

$$258 \quad \cos(\gamma) \approx \frac{S_1 - S_3}{E[x^2] - E[v^2]}$$

259 and therefore, it is sensible to:

$$260 \quad \text{reject bimodality for } \textit{small} \text{ values of } S_1 - S_3. \quad (5)$$

261 Further algebra shows that

$$262 \quad T_{11} - T_{33} = \cos(\gamma) \{E[x^4] - E[v^4]\}, \quad (6)$$

263 where T_{11} and T_{33} are the population versions of S_{11} and S_{33} , respectively. Then (6) gives

$$264 \quad \cos(\gamma) \approx \frac{S_{11} - S_{33}}{E[x^4] - E[v^4]}$$

265 and so, it is sensible to:

$$266 \quad \text{reject bimodality for } \textit{small} \text{ values of } S_{11} - S_{33}. \quad (7)$$

267 The significance of tests (5) or (7) is assessed by comparing the observed value of the statistic
 268 with the randomisation distribution. This is achieved by creating a further B pseudo-samples
 269 (for a suitable positive integer B), in each of which the i th observation is obtained from $\pm x_i$ by
 270 rotating $\pm x_i$ about the closer of the 2 fitted modes through a uniformly distributed random
 271 angle. The p -value is taken as the proportion of the $B+1$ values of the statistic that are smaller
 272 than (or equal to) the observed value.

273

274 4.3 Results for synthetic datasets

275 Table 1 gives the p -values and corresponding decisions (at the 5% level) obtained by applying
 276 the tests to some synthetic datasets simulated from the bimodal equal mixture model. Table 2
 277 does the same for some datasets simulated from the quadrimodal equal mixture model. In each
 278 case, both tests come to the correct conclusion.

| True number of modes | κ | n | $S_1 - S_3$ test | | $S_{11} - S_{33}$ test | |
|-------------------------|----------|-----|------------------|------------|------------------------|------------|
| | | | p -value | # of modes | p -value | # of modes |
| 2 | 10 | 52 | 0.37 | 2 | 0.51 | 2 |
| 2 | 10 | 360 | 0.27 | 2 | 0.33 | 2 |
| 2 | 20 | 52 | 0.66 | 2 | 0.69 | 2 |
| 2 | 20 | 360 | 0.20 | 2 | 0.25 | 2 |
| 2 | 50 | 52 | 0.45 | 2 | 0.48 | 2 |
| 2 | 50 | 360 | 0.35 | 2 | 0.42 | 2 |
| 2 | 100 | 52 | 0.34 | 2 | 0.41 | 2 |

| | | | | | | |
|---|-----|-----|------|---|------|---|
| 2 | 100 | 360 | 0.60 | 2 | 0.63 | 2 |
|---|-----|-----|------|---|------|---|

279

280 **Table 1.** p -values and corresponding decisions at 5% significance level of randomisation tests
 281 of bimodality for bimodal equal mixtures of synthetic Watson distributions. n =total sample size.
 282 $B=999$ further randomisation samples per data set (see text for details).

283

| True number of modes | $S_1 - S_3$ test | | | | $S_{11} - S_{33}$ test | |
|-------------------------|------------------|-----|------------|------------|------------------------|------------|
| | κ | n | p -value | # of modes | p -value | # of modes |
| 4 | 10 | 52 | 0.00 | > 2 | 0.00 | > 2 |
| 4 | 10 | 360 | 0.00 | > 2 | 0.00 | > 2 |
| 4 | 20 | 52 | 0.00 | > 2 | 0.00 | > 2 |
| 4 | 20 | 360 | 0.00 | > 2 | 0.00 | > 2 |
| 4 | 50 | 52 | 0.00 | > 2 | 0.00 | > 2 |
| 4 | 50 | 360 | 0.00 | > 2 | 0.00 | > 2 |
| 4 | 100 | 52 | 0.00 | > 2 | 0.00 | > 2 |
| 4 | 100 | 360 | 0.00 | > 2 | 0.00 | > 2 |

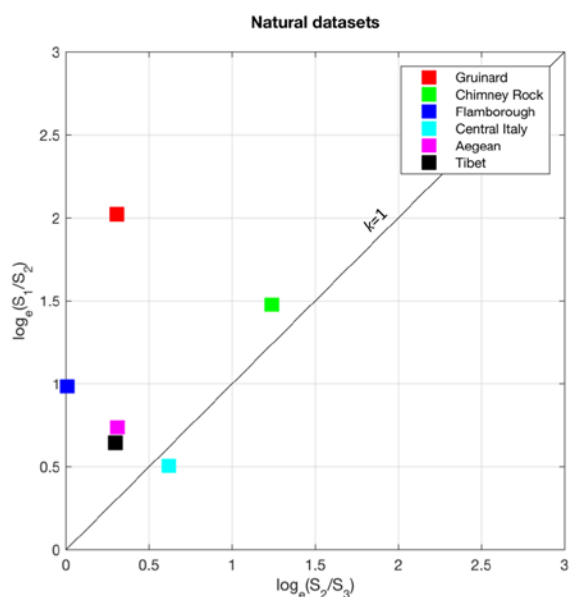
284

285 **Table 2.** p -values and corresponding decisions at 5% significance level of randomisation tests
 286 of bimodality for quadrimodal equal mixtures of Watson distributions. n =total sample size.
 287 $B=999$ further randomisation samples per data set (see text for details).

288

289 *4.4 Results for natural datasets*

290 Table 3 gives the p -values and corresponding decisions (at the 5% level) obtained by applying
 291 the tests to the natural datasets discussed in Section 3.2. For each dataset, the two tests come
 292 to the same conclusion, which is plausible in view of Figure 5. Figure 7 shows the fabric
 293 eigenvalue plot for these datasets.



294

295 **Figure 7.** Eigenvalue ratio plot for the natural datasets shown in Figure 5. All but one dataset
 296 (Central Italy) lies above the line for $k=1$. The best-constrained quadrimodal fault dataset
 297 (Gruinard) has the highest ratio of $\log_e(S_1/S_2)$.

298

| Field location | $S_1 - S_3$ test | | | $S_{11} - S_{33}$ test | |
|----------------------|------------------|------------|------------|------------------------|------------|
| | n | p -value | # of modes | p -value | # of modes |
| Gruinard | 75 | 0.00 | > 2 | 0.00 | > 2 |
| Chimney Rock | 86 | 0.99 | 2 | 1.00 | 2 |
| Flamborough | 346 | 0.00 | > 2 | 0.00 | > 2 |
| Central Italy | 1182 | 0.00 | > 2 | 0.00 | > 2 |
| Aegean | 156 | 0.00 | > 2 | 0.00 | > 2 |
| Tibet | 168 | 0.00 | > 2 | 0.00 | > 2 |

299

300 **Table 3.** p -values and corresponding decisions at 5% significance level of randomisation tests
 301 of bimodality for natural data sets. n =total sample size. $B=999$ further randomisation samples
 302 per data set (see text for details).

303

304 5. Discussion

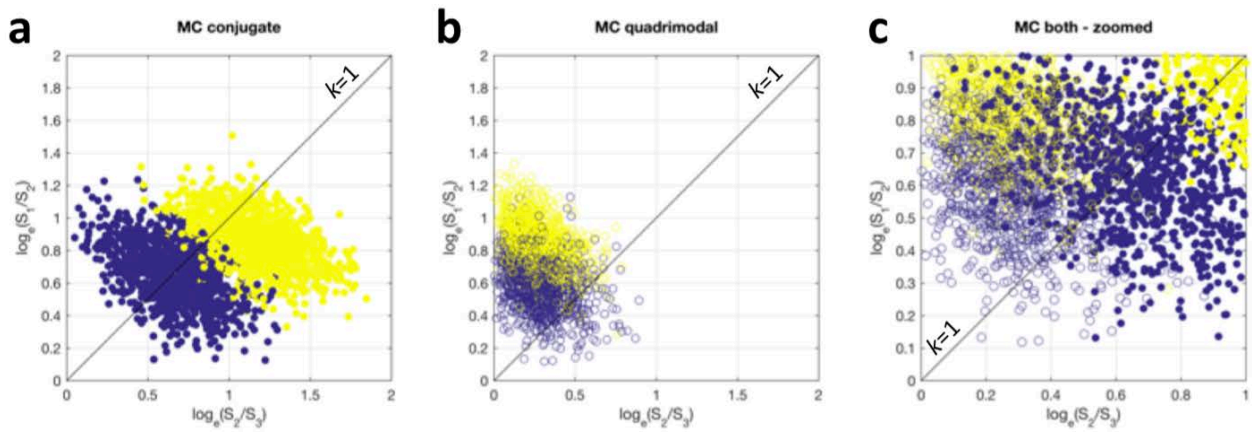
305 In the analysis described above and the tests we performed with synthetic datasets, we
 306 assumed that bimodal and quadrimodal Watson orientation distributions provide a reasonable
 307 approximation to the distributions of poles to natural fault planes. In terms of the underlying
 308 statistics this is unproven, but we know of no compelling evidence in support of alternative
 309 distributions. New data from carefully controlled laboratory experiments on rock or analogous

310 materials might provide important constraints for the underlying statistics of shear fracture
311 plane orientations.

312 We have tested our new methods on synthetic and natural datasets. Arguably, six natural
313 datasets are insufficient to establish firmly the primacy of polymodal orthorhombic fault
314 patterns in nature (Figure 7). However, we reiterate the key recommendation from Healy et al.
315 (2015): to be useful for this task, fault orientation datasets need to show clear evidence of
316 contemporaneity among all fault sets, through tools such as matrices of cross-cutting
317 relationships (Potts & Reddy, 2000). In addition, as shown above, larger datasets ($n > 200$) tend
318 to show clearer patterns. Scope exists to collect fault or shear fracture orientation data from
319 sources other than outcrops: Yielding (2016) has measured normal faults in seismic reflection
320 data from the North Sea and Ghaffari et al. (2014) measured faults in cm-sized samples
321 deformed in the laboratory and then scanned by X-ray computerised tomography.

322 The Chimney Rock dataset is probably not orthorhombic according to the two tests, and lies
323 close to the line for $k=1$ on Figure 7. It is interesting to note that the Chimney Rock data, and
324 other fault patterns from the San Rafael area of Utah, are considered as displaying
325 orthorhombic symmetry by Krantz (1989) and Reches (1978). However, a subsequent re-
326 interpretation by Davatzes et al. (2003) has ascribed the fault pattern to overprinting of earlier
327 deformation bands by later sheared joints. This may account for the inconsistent results of our
328 tests when compared to the position of the pattern on the eigenvalue plot. The Central Italy
329 dataset (taken from Roberts, 2007) is very large ($n=1182$) and the data were measured over a
330 wide geographical area. The dataset lies below the line for $k=1$ on the fabric eigenvalue plot
331 (Figure 7), which might suggest it is bimodal. However, for fault planes measured over large
332 areas there is a significant chance that regional stress variations may have produced
333 systematically varying orientations of fault planes.

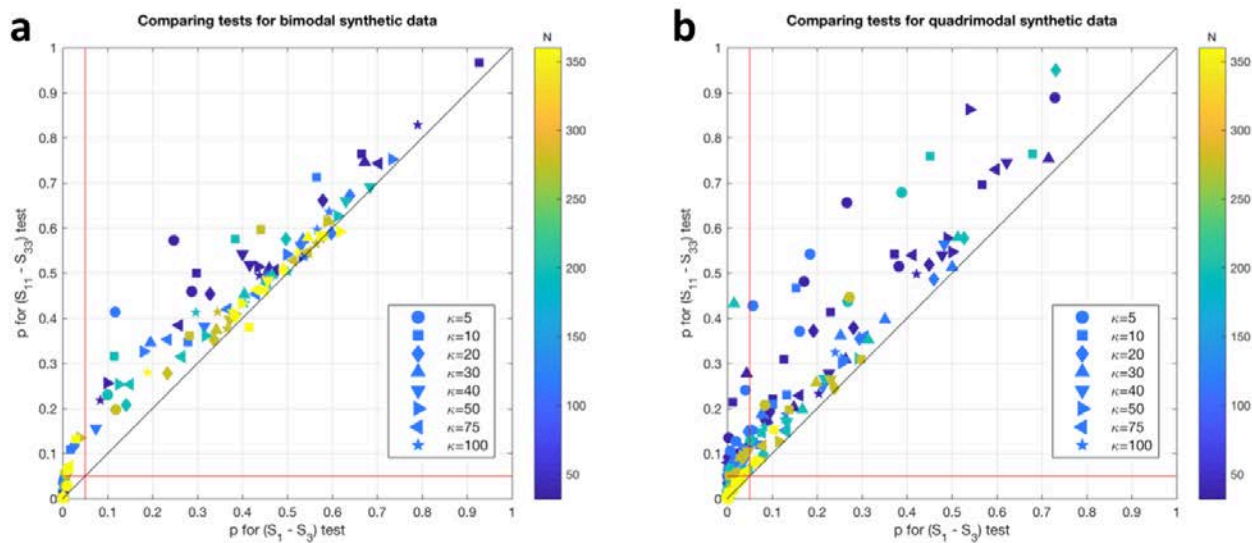
334 A final point concerns dispersion (noise) in the data. Synthetic datasets of bimodal (conjugate)
335 and quadrimodal patterns with low values of κ , the Watson concentration parameter, fall into
336 overlapping fields on the eigenvalue fabric plot. We ran 1000 Monte Carlo simulations of
337 bimodal and quadrimodal Watson distributions each with $n=52$ poles, and $\kappa=5$ and 10, and the
338 results are shown in Figure 8. Bimodal (conjugate) datasets for these dispersed and sparse
339 patterns lie across the 1:1 line on the fabric plot (Figure 8a; $\kappa=5$ in blue, $\kappa=10$ in yellow).
340 Quadrimodal datasets for these parameters are also noisy, with some fabrics lying below the
341 1:1 line (Figure 8b; $\kappa=5$ in blue, $\kappa=10$ in yellow). Under these conditions of low κ (dispersed)
342 and low n (sparse), it can be difficult to separate bimodal (conjugate) from quadrimodal fault
343 patterns. However, we assert that this may not matter: a noisy and dispersed 'bimodal'
344 conjugate fault pattern is in effect similar to a polymodal pattern i.e. slip on these dispersed
345 fault planes will produce a bulk 3D triaxial strain.



346

347 **Figure 8.** Eigenvalue ratio plots of synthetic data to illustrate the impact of dispersion on the
 348 ability of this plot to discriminate between conjugate (bimodal) and quadrimodal fault data. **a)**
 349 Monte Carlo ensemble of 2000 conjugate fault populations (mixtures of two equal Watson
 350 distributions), with κ varying from 5 (dark blue) to 10 (yellow). **b)** Monte Carlo ensemble of
 351 2000 quadrimodal fault populations (mixtures of four equal Watson distributions), with κ
 352 varying from 5 (dark blue) to 10 (yellow). **c)** Data from a) and b) merged onto the same plot
 353 and enlarged to show the region close to the origin. Note the considerable overlap between the
 354 conjugate (bimodal) data with the quadrimodal data, especially for $\kappa = 5$ (dark blue).

355 To assess the relative performance of the two tests presented in this paper, we generated
 356 synthetic bimodal and quadrimodal distributions and compared the resulting p-values from
 357 applying both the S_1 - S_3 and S_{11} - S_{33} tests to the same data. The results are shown in Figure 9,
 358 displayed as cross-plots of $p(S_1-S_3)$ versus $p(S_{11}-S_{33})$. While there is a slight tendency for the p-
 359 values from the S_{11} - S_{33} test to exceed those of the S_1 - S_3 test (i.e. the points tend on average to
 360 plot above the 1:1 line), neither of the tests can be said to 'better' or more 'accurate'. We
 361 therefore recommend the S_1 - S_3 test as simpler and sufficient.



362

363 **Figure 9.** Eigenvalue ratio plots comparing the relative performance of the two tests proposed
 364 in this paper. The red lines denote p-values for either test at $p=0.05$, and the diagonal black line
 365 is the locus of points where $p(S_1-S_3) = p(S_{11}-S_{33})$. **a)** For bimodal synthetic datasets with size

366 (N) varying from 32-360 and concentration (κ) varying from 5-100, both tests perform well
367 and reject the majority of the datasets ($p \gg 0.05$). The p-values for the S_{11} - S_{33} test are, on
368 average, slightly higher than those for the S_1 - S_3 test across a range of dataset sizes and
369 concentrations. **b)** For quadrimodal synthetic datasets, many of the p-values are < 0.05 , and this
370 especially true for the larger datasets (higher N, green/yellow). Smaller datasets (blue) can
371 return p-values > 0.05 .

372

373 **6. Summary**

374 Bimodal (conjugate) fault patterns form in response to a bulk plane strain with no extension in
375 the direction parallel to the mutual intersection of the two fault sets. Quadrimodal and
376 polymodal faults form in response to bulk triaxial strains and constitute the more general case
377 for brittle deformation on a curved Earth (Healy et al., 2015). In this contribution, we show that
378 distinguishing bimodal from quadrimodal fault patterns based on the orientation distribution
379 of their poles can be achieved through the eigenvalues of the 2nd and 4th rank orientation
380 tensors. We present new methods and new open source software written in R to test for these
381 patterns. Tests on synthetic datasets where we controlled the underlying distribution to be
382 either bimodal (i.e. conjugate) or quadrimodal (i.e. polymodal, orthorhombic) demonstrate that
383 a combination of fabric eigenvalue (modified Flinn) plots and our new randomisation tests can
384 succeed. Applying the methods to natural datasets from a variety of extensional normal-fault
385 settings shows that 5 out of the 6 fault patterns considered here are probably polymodal. The
386 most tightly constrained natural dataset (Gruinard) displays clear orthorhombic symmetry and
387 is unequivocally polymodal. Most map-scale natural faults evolve and grow through
388 interaction, splaying and coalescence, and in some cases through reactivation under stress
389 rotation. Variation within fault orientation datasets is therefore inherent. Statistical tests can
390 help to discern this variation and guide the interpretation of any underlying pattern. We
391 encourage other workers to apply these tests to their own data and assess the symmetry in the
392 brittle fault pattern and to consider what this means for the causative deformation.

393

394 **Acknowledgements**

395 DH gratefully acknowledges receipt of NERC grant NE/N003063/1, and thanks the School of
396 Geosciences at the University of Aberdeen for accommodating a period of research study leave,
397 during which time this paper was written. We thank two anonymous reviewers, plus Atilla
398 Aydin (Stanford) and Nigel Woodcock (Cambridge) for comments which helped us improve the
399 paper.

400

401 **References**

402 Aydin, A., and Reches, Z.E.: Number and orientation of fault sets in the field and in experiments.
403 *Geology*, 10(2), 107-112, 1982.

- 404 Blenkinsop, T. G.: Relationships between faults, extension fractures and veins, and stress.
405 *Journal of Structural Geology*, 30(5), 622-632, 2008.
- 406 Davatzes, N.C., Aydin, A. and Eichhubl, P.: Overprinting faulting mechanisms during the
407 development of multiple fault sets in sandstone, Chimney Rock fault array, Utah, USA.
408 *Tectonophysics*, 363(1-2), pp.1-18, 2003.
- 409 Ekström, G., Nettles, M., and Dziewoński, A. M.: The global CMT project 2004–2010: Centroid-
410 moment tensors for 13,017 earthquakes. *Physics of the Earth and Planetary Interiors*, 200, 1-9,
411 2012.
- 412 Fisher, N.I., Lewis, T. and Embleton, B.J.: *Statistical analysis of spherical data*. Cambridge
413 University Press, 1987.
- 414 Flinn, D.: On folding during three-dimensional progressive deformation. *Quarterly Journal of the*
415 *Geological Society*, 118(1-4), 385-428, 1962.
- 416 Ghaffari, H. O., Nasser, M. H. B., and Young, R. P.: Faulting of Rocks in a Three-Dimensional
417 Stress Field by Micro-Anticracks. *Scientific reports*, 4, 5011, 2014.
- 418 Healy, D., Jones, R.R. and Holdsworth, R.E.: Three-dimensional brittle shear fracturing by tensile
419 crack interaction. *Nature*, 439(7072), pp.64-67, 2006a.
- 420 Healy, D., Jones, R.R. and Holdsworth, R.E.: New insights into the development of brittle shear
421 fractures from a 3-D numerical model of microcrack interaction. *Earth and Planetary Science*
422 *Letters*, 249(1), pp.14-28, 2006b.
- 423 Healy, D., Blenkinsop, T.G., Timms, N.E., Meredith, P.G., Mitchell, T.M. and Cooke, M.L.:
424 Polymodal faulting: Time for a new angle on shear failure. *Journal of Structural Geology*, 80,
425 pp.57-71, 2015.
- 426 Krantz, R. W.: Orthorhombic fault patterns: the odd axis model and slip vector orientations.
427 *Tectonics*, 8(3), 483-495, 1989.
- 428 Lisle, R. J., and Leyshon, P. R.: *Stereographic projection techniques for geologists and civil*
429 *engineers*. Cambridge University Press, 2004.
- 430 Mardia, K.V. and Jupp, P.E.: *Directional statistics*. John Wiley & Sons, 2000.
- 431 McCormack, K.D. and McClay, K.R.: Orthorhombic faulting in the Beagle Sub-basin, North West
432 Shelf, Australia. *Geological Society, London, Special Publications*, 476, 2018.
- 433 Peacock, D. C. P., and Sanderson, D. J.: Effects of layering and anisotropy on fault geometry.
434 *Journal of the Geological Society*, 149(5), 793-802, 1992.
- 435 Potts, G. J., and Reddy, S. M.: Application of younging tables to the construction of relative
436 deformation histories—1: fracture systems. *Journal of Structural Geology*, 22(10), 1473-1490,
437 2000.

438 R Core Team: *R: A language and environment for statistical computing*. R Foundation for
439 Statistical Computing, Vienna, Austria. URL <https://www.R-project.org/>, 2017.

440 Ramsay, J.: *Folding and fracturing of rocks*, 1967.

441 Reches, Z. E.: Analysis of faulting in three-dimensional strain field. *Tectonophysics*, 47(1-2), 109-
442 129, 1978.

443 Reches, Z. E.: Faulting of rocks in three-dimensional strain fields II. Theoretical analysis.
444 *Tectonophysics*, 95(1-2), 133-156, 1983.

445 Reches, Z. E., and Dieterich, J. H.: Faulting of rocks in three-dimensional strain fields I. Failure
446 of rocks in polyaxial, servo-control experiments. *Tectonophysics*, 95(1-2), 111-132, 1983.

447 Roberts, G. P.: Fault orientation variations along the strike of active normal fault systems in Italy
448 and Greece: Implications for predicting the orientations of subseismic-resolution faults in
449 hydrocarbon reservoirs. *AAPG bulletin*, 91(1), 1-20, 2007.

450 Scheidegger, A. E.: On the statistics of the orientation of bedding planes, grain axes, and similar
451 sedimentological data. *US Geological Survey Professional Paper*, 525, 164-167, 1965.

452 Woodcock, N.H.: Specification of fabric shapes using an eigenvalue method. *Geological Society
453 of America Bulletin*, 88(9), pp.1231-1236, 1977.

454 Yielding, G.: The geometry of branch lines. In: Childs, C., Holdsworth, R. E., Jackson, C. A.-L.,
455 Manzocchi, T., Walsh, J. J. & Yielding, G. (eds). *The Geometry and Growth of Normal Faults*.
456 Geological Society, London, Special Publications, 439, 2016.

457